Tailored hardening of ZrCuAl bulk metallic glass induced by 2D gradient rejuvenation

Wookha Ryu [1], Rui Yamada[1] and Junji Saida [1]

Abstract

The work hardening behavior of bulk metallic glasses has not been previously ascribed to their intrinsic structure but rather to the introduction of other components that act as hardening elements. Here, we present clear evidence of a 2D gradient rejuvenation state that can induce tailored hardening of a monolithic bulk metallic glass. We show that the local free volume content related to the rejuvenation state controls the shear band angle and the maximum effective shear stress. Hence, shear band propagation is prohibited, and the formation of a complete shear plane transecting the whole specimen is blocked. The generation of plastic strain is accompanied by an increase in the critical shear stress, resulting in sustainable apparent hardening. In this way, we present a bulk metallic glass that has a tailored hardening mechanism and establish an experimental link between a gradient rejuvenation state and mechanical properties.

Introduction

Work softening behavior can lead to catastrophic failure through localized stresses at the site of deformation. Although bulk metallic glasses (BMGs) have attracted much attention owing to their high strength and wide elastic limit[1–3], a major disadvantage in terms of their mechanical properties is intrinsic work softening[4–6]. Therefore, studies to realize work hardening in BMGs have been actively conducted by introducing other components with work hardening elements, such as an austenite secondary phase, transformable heterogeneities, and geometric imperfections[7–13].

Apparent work hardening of a monolithic BMG is achieved only under specific conditions[14,15]. Generally, incomplete shear bands can be readily observed at surface flaws or in soft regions even when the applied stress is lower than the yield strength of the material[11,14,16–19]. The plastic strain of these materials apparently increases in response to the initiation and progressive propagation of shear bands. Moreover, the strength of these materials increases as the deformation proceeds, which is

considered to be apparent hardening[7,8,15]. Shear bands are sequentially activated from sites with low critical shear stress to those with high critical shear stress. Hence, subsequent shear banding requires a higher applied stress than previous shear banding[20,21]. When a complete shear plane transects the specimen upon macroscopic yielding, plastic deformation proceeds through shear sliding, and no further apparent hardening occurs[15]. Because the local critical shear stress over the entire area of the complete shear plane is less than the shear stress already applied, simultaneous sliding occurs in the complete shear plane. Thus, plastic deformation can be continuously generated without activating shear banding at new sites with higher critical shear stress[20–22].

The apparent hardening mechanism of monolithic BMGs was not believed to substantially contribute to plastic deformation after macroscopic yielding. However, we posit that if a complete shear band is not formed, an alternative hardening mechanism of BMGs might occur even after macroscopic yielding where shear banding is continuously activated at new sites with higher critical shear stress. Here, we present experimental evidence for the tailored hardening behavior of monolithic BMGs throughout the overall plastic deformation stage.

Correspondence: Wookha Ryu (ldsruh07@gmail.com)
[1]Frontier Research Institute for Interdisciplinary Sciences (FRIS), Tohoku University, Sendai, Japan

Asymmetric cryogenic heat treatment of a BMG generates 2D gradient rejuvenation, i.e., a gradient of the free volume content in a specific direction of the sample. A notable difference in the local free volume changes the angle of the shear band initiation and propagation, thereby completely preventing the formation of a complete shear plane.

Materials and methods
Alloy fabrication
Ingots of $Zr_{60}Cu_{30}Al_{10}$ (at.%) alloy were prepared by arc-plasma remelting elements with high purity (higher than 99.9 wt.%). The materials were remelted at least 5 times under a Ti-gettered Ar atmosphere to ensure chemical homogeneity. Cylindrical samples with a diameter of 4 mm were fabricated by casting in a Cu mold.

Heat treatment
Each BMG sample was covered by two Cu jigs on the sample stage. Under high vacuum ($P \approx 2 \times 10^{-3}$ Pa), the sample was heated to approximately $1.04T_g$ at a heating rate of 0.4 K/s by the heater on the upper Cu jig and held isothermally for 2 min. Then, the sample stage moved to contact the liquid N_2 (LN_2)-cooled Cu mesh. The lower Cu jig contacted the Cu mesh to cool the BMG sample. The upper and lower Cu jigs were spaced 90 μm apart. The temperatures at the top and bottom of the BMG sample were measured with a thermocouple. The densities of the top and bottom parts of the heat-treated specimens with a mass greater than 1.0 g were measured by the Archimedes principle, for which the accuracy was ±0.005 g/cm³. The BMG sample was then relaxed by annealing for 2 min at 700 K at heating and cooling rates of 0.4 K/s. Although thermal cycling potentially effects the mechanical properties and atomic structure of a material[23], in the case of high-temperature heat treatment, it is difficult to perform repeated tests because of the risk of crystallization.

Differential scanning calorimetry (DSC) measurements
The specific heat (C_p), glass transition temperature (T_g), and onset crystallization temperature (T_x) of each sample were measured on a differential scanning calorimeter (PerkinElmer Pyris Diamond DSC) at a heating rate of 20 K/min.

Scanning electron microscopy (SEM) imaging
The fracture and side surfaces of the compressed samples were observed with a scanning electron microscope (JEOL JSM-7100F).

Compression testing
The mechanical behavior of each sample during compression was investigated with the use of an Instron 5982 testing machine at a constant strain rate of 2×10^{-4}/s; each specimen used for these tests had a diameter of 4 mm and an aspect ratio of approximately 1:2. For SEM observations, the compressive deformation was interrupted after 2.5% plastic strain. Five as-cast samples and five heat-treated samples were tested to ensure reproducibility.
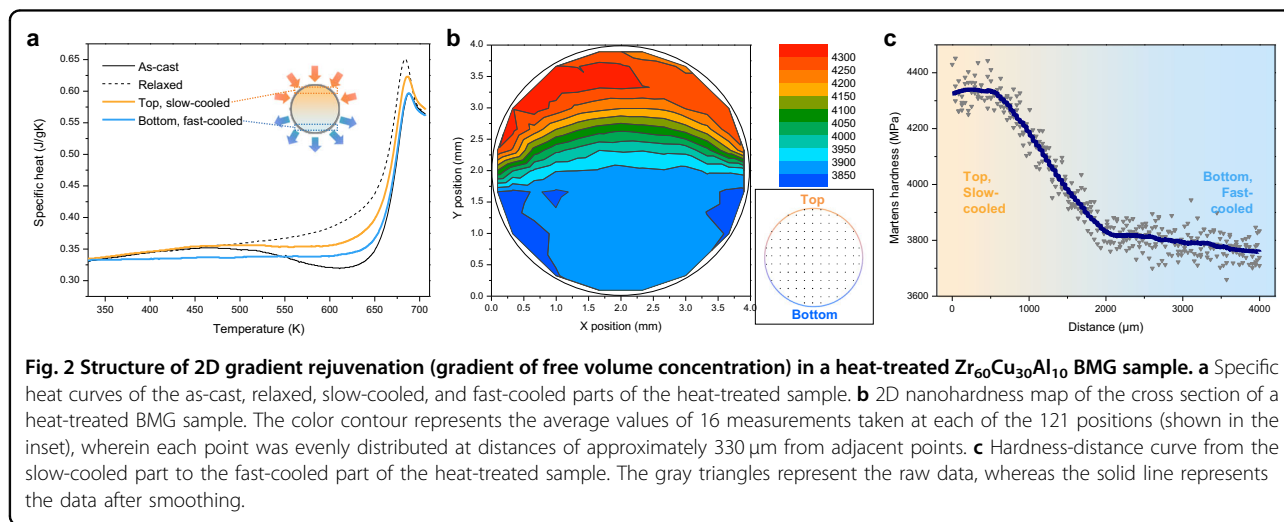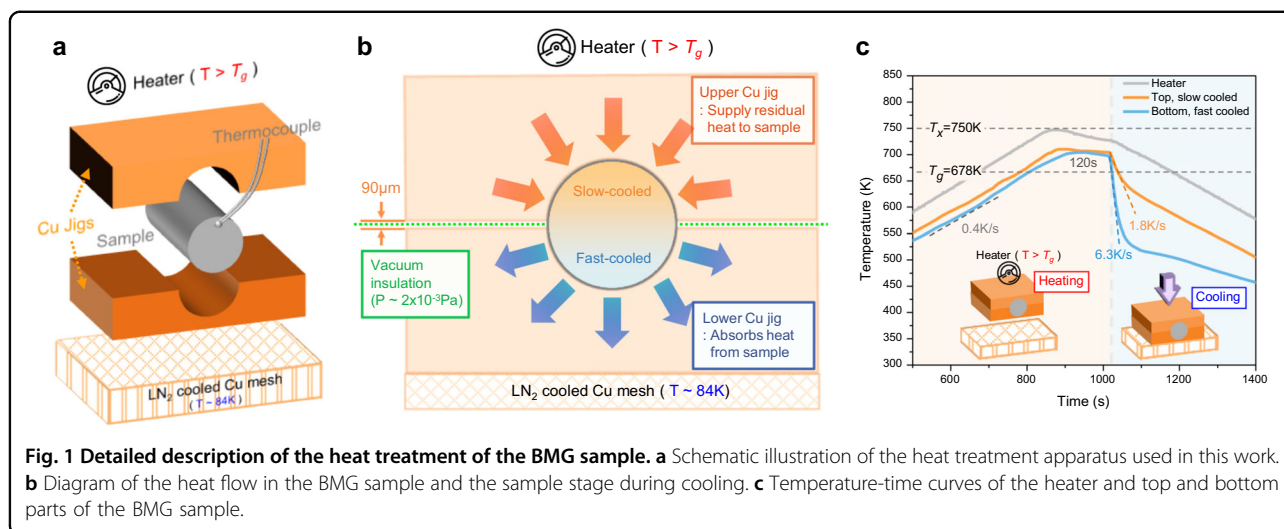
Nanoindentation test
Nanoindentation measurements were performed at a peak load of 100 mN, where the loading and unloading rate was 10 mN/s. For the 2D nanohardness maps of the cross section of the heat-treated BMG samples, indentation tests were repeated 16 times to obtain average values for 121 different positions. The 121 positions were evenly distributed with a distance of approximately 330 μm between adjacent points. For 1D line scanning, a total of 300 indentations were taken from the slow-cooled part to the fast-cooled part. The α and θ_c values were interpolated according to the nanohardness change based on the shear band angles of the slow-cooled and fast-cooled ends of the compressed sample.

Results and discussion
2D gradient rejuvenation in a monolithic BMG
The free volume content of a metallic glass is highly dependent on the cooling rate when cooling at temperatures above T_g[24–30]. To introduce a 2D gradient rejuvenation (gradient of free volume content) into a single BMG sample, a novel heat treatment apparatus was developed to achieve different cooling rates at the top and bottom parts of the specimen during cooling. Figure 1a shows a detailed description of the heat treatment apparatus used to introduce a 2D gradient rejuvenation into the cylindrical BMG samples. Each cylindrical BMG sample was covered with two Cu jigs. The vertical movement of the Cu jigs was controlled by a motor, and the jigs were located at the top side during heating and at the bottom side during cooling. The upper jig was heated through a physical connection with the heater and supplied heat to the BMG sample and the lower jig. Upon cooling, the lower jig contacted an LN_2-cooled Cu mesh located below the jig to cool the BMG sample and the upper jig. The upper and lower jigs were not in direct contact with each other; they were separated by 90 μm. Because the heat treatment was performed under a high vacuum atmosphere, both Cu jigs were insulated from each other, and thermal conduction was achieved only through the BMG sample, as shown in Fig. 1b. The bottom part of the BMG sample was quenched by the lower Cu jig during cooling; however, the top part was cooled at a relatively slow cooling rate because the upper Cu jig continuously supplied residual heat. The thermal history of a $Zr_{60}Cu_{30}Al_{10}$ cylindrical BMG sample with a diameter of 4 mm was measured by thermocouples attached

Fig. 1 Detailed description of the heat treatment of the BMG sample. a Schematic illustration of the heat treatment apparatus used in this work. **b** Diagram of the heat flow in the BMG sample and the sample stage during cooling. **c** Temperature-time curves of the heater and top and bottom parts of the BMG sample.

Fig. 2 Structure of 2D gradient rejuvenation (gradient of free volume concentration) in a heat-treated $Zr_{60}Cu_{30}Al_{10}$ BMG sample. a Specific heat curves of the as-cast, relaxed, slow-cooled, and fast-cooled parts of the heat-treated sample. **b** 2D nanohardness map of the cross section of a heat-treated BMG sample. The color contour represents the average values of 16 measurements taken at each of the 121 positions (shown in the inset), wherein each point was evenly distributed at distances of approximately 330 μm from adjacent points. **c** Hardness-distance curve from the slow-cooled part to the fast-cooled part of the heat-treated sample. The gray triangles represent the raw data, whereas the solid line represents the data after smoothing.

to the top and bottom parts, as shown in Fig. 1c. Cooling was performed after isothermal holding for 2 min at approximately $1.04T_g$. The initial cooling rates of the top and bottom parts of the sample were 1.8 K/s and 6.3 K/s, respectively.

To measure the thermal properties of the specimens after the heat treatment, the top part (approximately 200–800 μm from the top) and the bottom part (approximately 200–800 μm from the bottom) were analyzed by DSC. Figure 2a shows the results of specific heat measurements of the as-cast BMG and the top and bottom parts of the heat-treated sample. The specific heat of the top part of the heat-treated sample was higher than that of the bottom part, which suggests the formation of a glassy structure with a relatively small free volume content. The densities of the top and bottom parts of the sample were 6.496 g/cm^3 and 6.471 g/cm^3, respectively.

The difference in the average value of the density was approximately 0.39%, which directly showed that the contents of the free volume at the top and bottom of the heat-treated specimen were different.

A 2D indentation map was constructed to investigate the difference in free volume content in the heat-treated BMG specimen. Figure 2b is a color contour map that shows the average value of the hardness measured at 121 different positions (shown inset) on the cross section of the 4 mm cylindrical sample. The high hardness of the top part was maintained up to a distance of 600 μm, after which it started to decrease sharply. From a distance of 2000 μm to the bottom part, the hardness exhibited little change. To measure the hardness gradient more specifically, 1D line scanning was performed, which comprised 300 indentations from the slow-cooled top part to the fast-cooled bottom part.
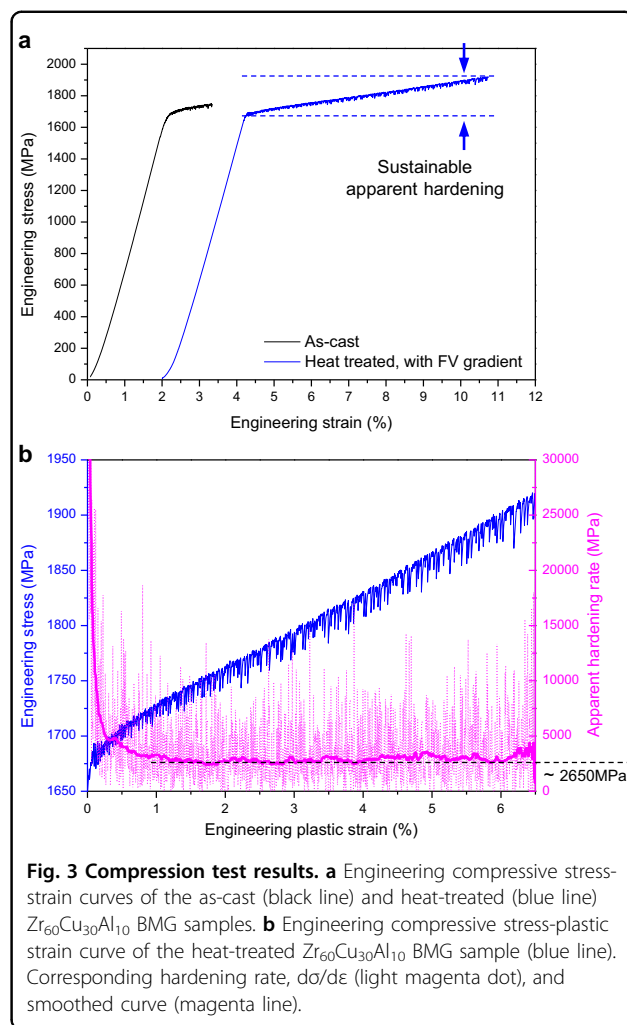
Figure 2c shows the raw hardness data (gray triangles) and the smoothed hardness (solid line). The high hardness of the top part was maintained up to a distance of 600 μm, after which it started to decrease sharply. From a distance of 2000 μm to the bottom part, the hardness tended to decrease slowly. The hardness value and specific heat reflect the difference in the local free volume content depending on the rejuvenation state. Due to the asymmetric cooling rate, residual stress may have been applied, which is reflected in the mechanical properties. The effect can be investigated by comparing it with a stress-free sample. In this regard, the hardness values of the as-cast and relaxed samples were measured to be 3997 ± 61 Pa and 4380 ± 84 Pa, respectively, which were comparable to the hardness of the slow-cooled and fast-cooled parts shown in Fig. 2c. Therefore, there may be an effect from residual stresses, but their influence was considered not dominant. Notably, a gradient of the free volume content was formed from the top to the bottom. In particular, a transition section in which the free volume content rapidly changed was formed in the section at distances from the surface in the range of 600–2000 μm.

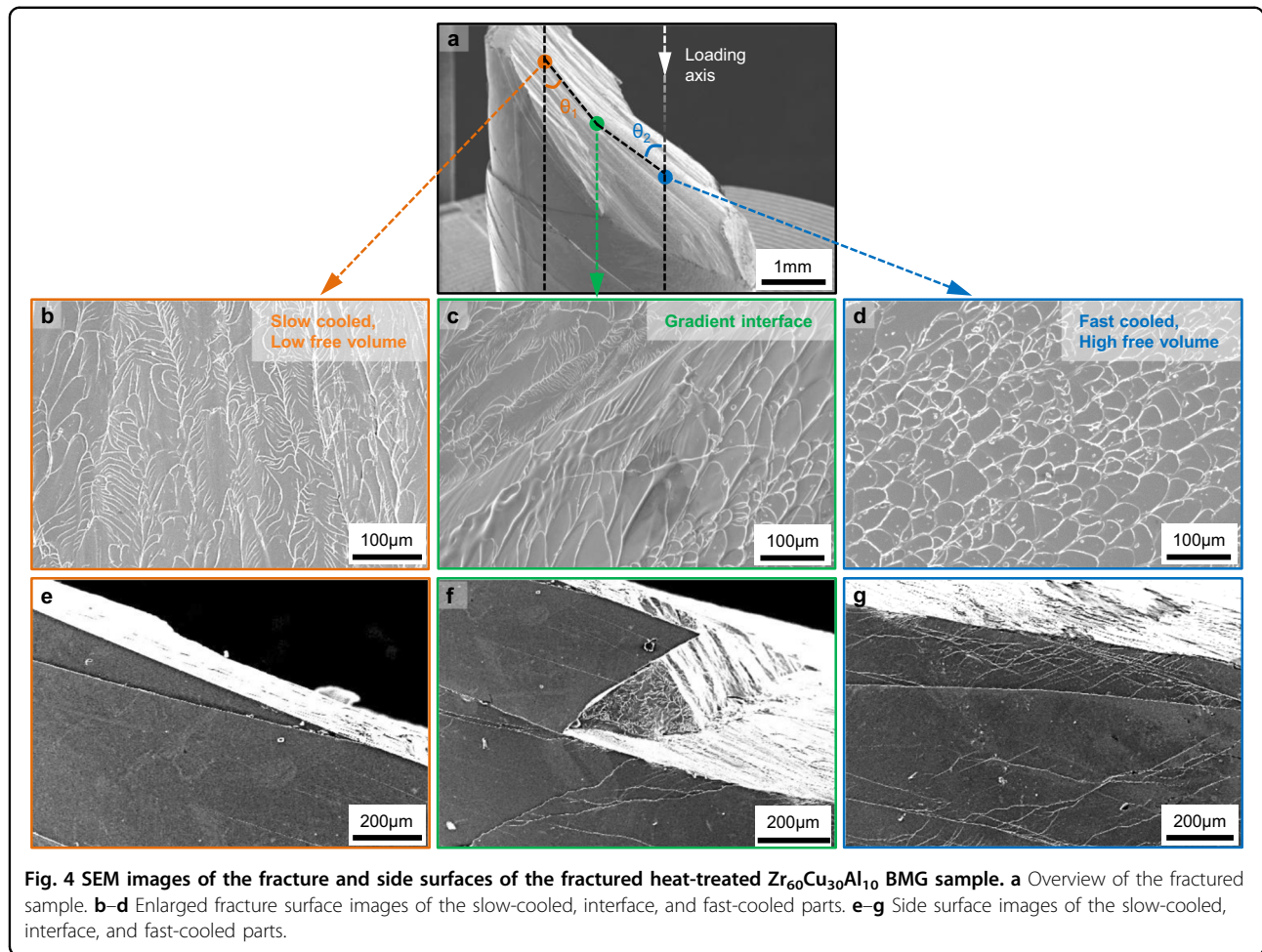## Mechanical properties of BMGs with 2D gradient rejuvenation

The compression test results of the as-cast and heat-treated $Zr_{60}Cu_{30}Al_{10}$ BMG samples are shown in Fig. 3a. According to five measurements from each specimen, the average and standard deviation of the plastic strains of the as-cast and heat-treated samples were 2.52 ± 0.63% and 7.21 ± 2.19%, respectively. The plastic strain was greatly increased by the introduction of 2D gradient rejuvenation. Notably, sustainable apparent hardening behavior (hardening rate, $d\sigma/d\varepsilon \approx 2650$ MPa) was observed in the plastic deformation zone of the engineering stress-strain curve of the heat-treated sample, as shown in Fig. 3b. Figure S1 also shows the true stress-strain curves, which were obtained by converting the engineering stress-strain values. Recent studies have suggested that the work hardening behavior of a BMG occurs by the formation of heterogeneities, such as short-range ordering, secondary crystalline phases capable of martensitic phase transformation, or notches and surface impressions[7,8,11–13]. In those cases, the hardening rate was relatively high just after yielding. As the plastic strain increased, hardening elements were consumed, and the work hardening rate tended to decrease sharply.

Shear band morphology

The deformation mechanism of a BMG can be investigated by observing the initiation and propagation pattern of the shear band. Notably, it has been reported that prohibition of shear band initiation and propagation is

Fig. 3 Compression test results. a Engineering compressive stress-strain curves of the as-cast (black line) and heat-treated (blue line) $Zr_{60}Cu_{30}Al_{10}$ BMG samples. **b** Engineering compressive stress-plastic strain curve of the heat-treated $Zr_{60}Cu_{30}Al_{10}$ BMG sample (blue line). Corresponding hardening rate, $d\sigma/d\varepsilon$ (light magenta dot), and smoothed curve (magenta line).

necessary to increase plasticity[14,15,31] and that apparent hardening phenomenon is accompanied by a shear band exhibited by the locally confined stress state[7,8,13]. As shown in Fig. 4, images of a fracture surface and side view of a fractured sample clearly show the difference of the local rejuvenation state, i.e., the difference in the local free volume content in the BMG sample. Figure 4a shows an overall view of a fractured sample. The top and bottom of the fracture surface were clearly separated from the roughness and shapes in the image. The slow-cooled top part exhibited typical viscous river-like patterns along the shear direction with a very narrow spacing (Fig. 4b). The fast-cooled bottom part exhibited a vein pattern observed in typical as-cast BMGs with a relatively wide spacing (Fig. 4d)[32,33]. In the image in Fig. 4c, narrow river-like and wide vein-like patterns appeared on both sides with a gap of a few hundred micrometers between them, indicating that the region corresponded to the interface between two different fracture surfaces. Very few shear bands were observed on

Fig. 4 SEM images of the fracture and side surfaces of the fractured heat-treated Zr$_{60}$Cu$_{30}$Al$_{10}$ BMG sample. a Overview of the fractured sample. **b–d** Enlarged fracture surface images of the slow-cooled, interface, and fast-cooled parts. **e–g** Side surface images of the slow-cooled, interface, and fast-cooled parts.

the upper side, and many primary and secondary shear bands were found on the lower side (Fig. 4e and g). An image of the side surface at the interface of regions with different free volume contents (Fig. 4f) showed that shear bands in various directions interacted before the fracture occurred. Additionally, the shear planes in various directions overlapped, thereby forming an irregular fracture surface.

The fracture angle of the top part ($\theta_1 = 40°$) was smaller than the angle of the bottom part ($\theta_2 = 44.1°$) (Fig. 4a). According to previously reported experimental results, the shear plane angle is in the range of 39.5°–44° under compressive loading for BMGs of various compositions[17,34]. The shear band plane and fracture surface of BMGs do not appear along the maximum shear stress direction but rather occur along the angle at which the corresponding effective shear stress is maximized. Here, the normal stress is reflected by atomic friction. According to the Mohr–Coulomb criterion, the respective equations of the effective shear stress τ_c and the critical applied stress for shear band formation σ_c are given as follows[17,34,35]:

$$\tau_c = \tau_0 - \alpha\sigma_n \tag{1}$$

and

$$\sigma_c = \frac{\tau_0}{\sin\theta \left(\cos\theta - \alpha\sin\theta\right)} \tag{2}$$

where τ_0 is a constant, σ_n is the normal stress, θ is the shear band angle between the shear plane and loading axis, and α is the normal stress coefficient. The normal stress coefficient can be given implicitly by the following expression:

$$\alpha = \frac{\cos\left(2\theta_c\right)}{\sin\left(2\theta_c\right)} \tag{3}$$

where θ_c is the shear band angle at which σ_c has a minimum value[36–39].

The greater the atomic friction is, the greater the effect of normal stress, and the smaller the shear band angle

during compressive deformation. The structural relaxation of metallic glass is associated with a reduction in free volume content by relaxation, leading to an increase in the atomic friction and the α value and a decrease in the shear band angle[34,36,37,39,40]. Therefore, the shear band angle in the slow-cooled top part should be smaller than that in the fast-cooled bottom part. In addition, the increase in atomic friction makes the initiation and propagation of the shear band more difficult[40]. Figure 4e clearly shows that a secondary shear band was hardly observed on the side surface of the top part owing to increased atomistic friction and a reduced free volume concentration.

The values of local α and θ_c are determined depending on the free volume. The σ_c is at a minimum when the shear band propagates at θ_c. Shear bands have been reported to propagate discretely in stages rather than continuously[15]. If θ_c changes at a particular stage during propagation, the shear band plane may form as a non-uniform surface with a bent shape. To experimentally verify our hypothesis, SEM images were taken of the side surfaces of the samples after fracture and interrupted compression. Figure 5a shows the side surface of a sample interrupted at plastic strain of 2.5%. The left and right sides of the image correspond to zones of low and high free volume concentrations. The primary shear band, which initiated at the upper left and propagated to the right, was deflected twice during propagation to form a bent shear plane, and further propagation was stopped. As the shear band progressed from left to right, it was deflected, creating a larger shear band angle, which indicates that θ_c was greater in regions with a high free volume content than in those with a low free volume content. Notably, branched shear bands were formed at tangential angles to both shear bands at the point of deflection. However, the shear band that initiated from the lower right and propagated to the left stopped without any obvious deflection. Hence, it is preferable for the shear band to stop rather than deflect and propagate when it progresses from a region of high to low free volume content. Figure 5b shows a schematic diagram of the shear band propagation and branching, which stopped when the two different shear bands initiated from the low and high free volume zones and propagated in opposite directions in a BMG sample with a gradient free volume content. The shear bands were interrupted during propagation before forming a flat and complete shear plane transecting the BMG sample. Upon further plastic deformation, other new shear bands initiated at new locations. Multiple shear bands intersected during propagation, which dissipated the shear stress in the shear plane. Therefore, the formation of a complete shear band became even more difficult, and the fracture was delayed. This effect promoted the subsequent initiation of new shear bands, which achieved a plastic deformation cycle (Fig. 5c). As a result,
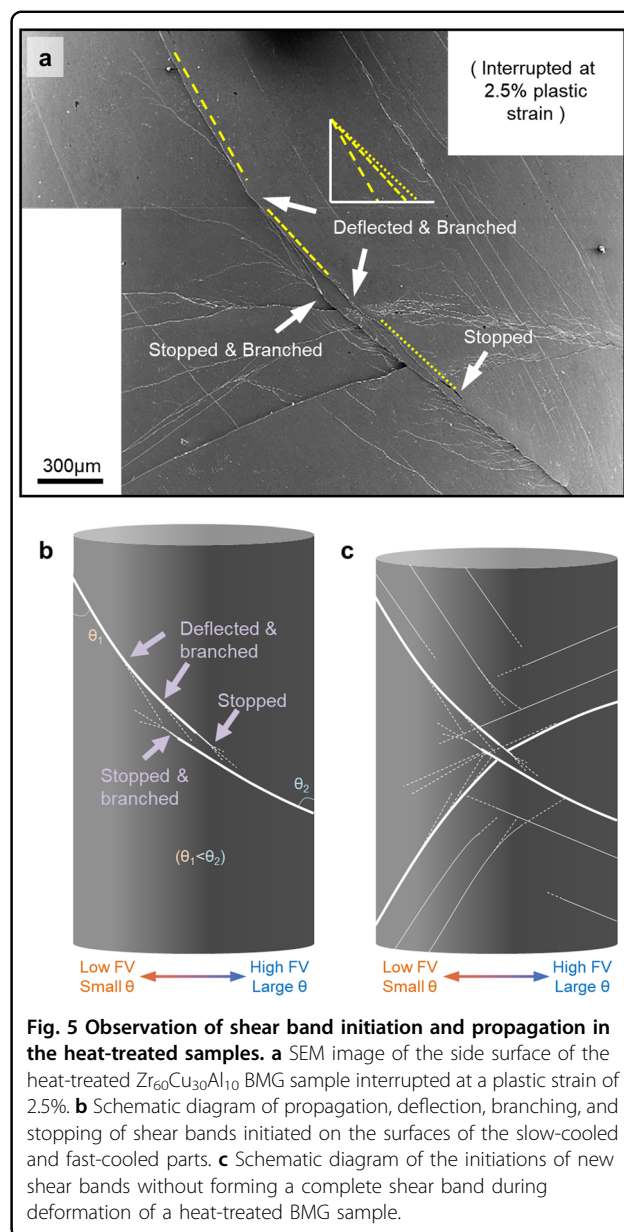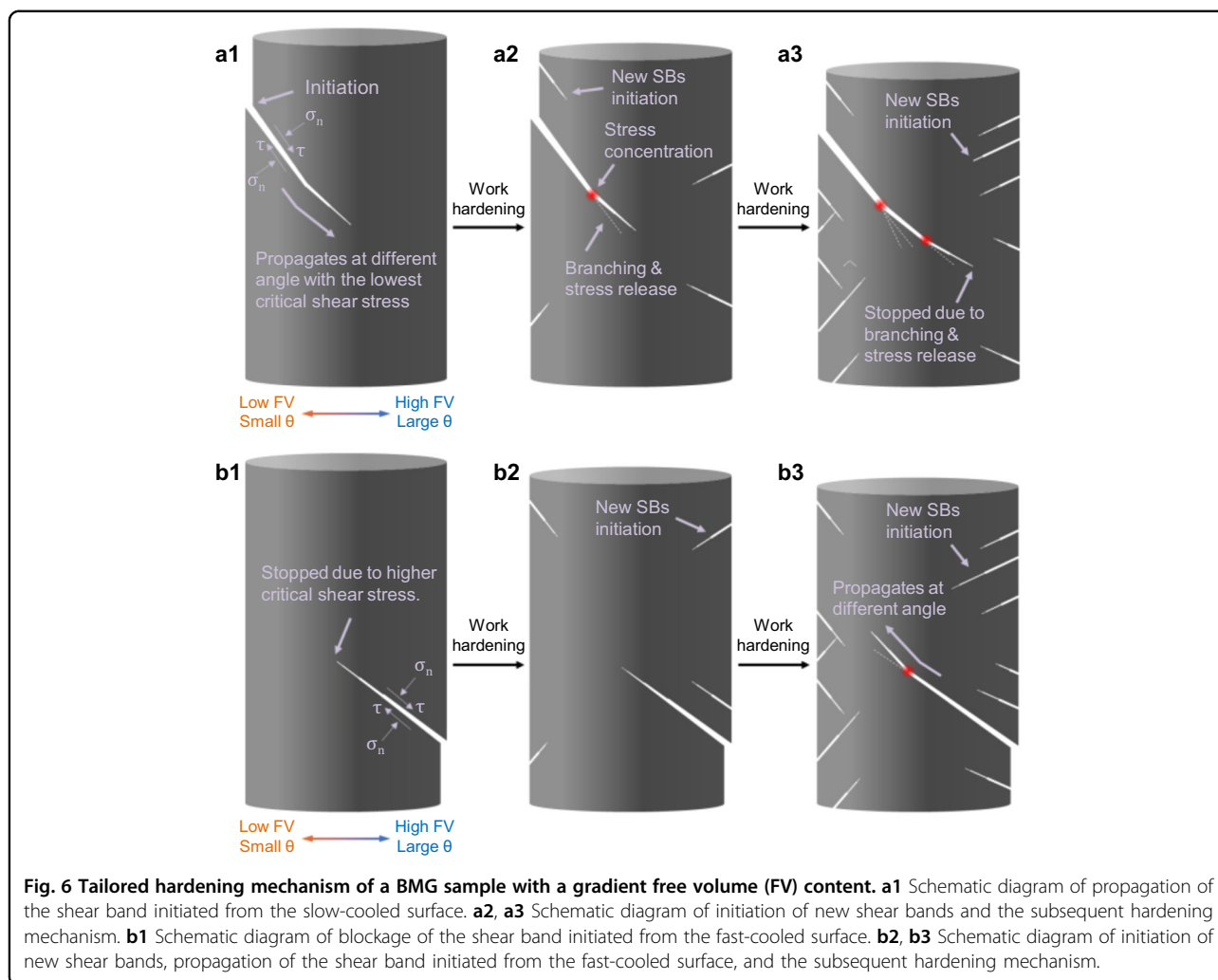

Fig. 5 Observation of shear band initiation and propagation in the heat-treated samples. a SEM image of the side surface of the heat-treated $Zr_{60}Cu_{30}Al_{10}$ BMG sample interrupted at a plastic strain of 2.5%. **b** Schematic diagram of propagation, deflection, branching, and stopping of shear bands initiated on the surfaces of the slow-cooled and fast-cooled parts. **c** Schematic diagram of the initiations of new shear bands without forming a complete shear band during deformation of a heat-treated BMG sample.

the plastic strain in the BMG sample was not caused by a large shear step at a particular major shear plane but rather by the generation of a large number of small incomplete shear bands.

Tailored hardening mechanism of BMGs by 2D gradient rejuvenation

Figure 6a1-a3 shows schematic illustrations of the propagation of shear bands initiated in the lower free volume region and the subsequent tailored hardening mechanism. When a shear band initiated at a heterogeneous site with a low critical shear stress by a surface flaw, the initial shear band formed at θ_c, which maximized the effective shear stress reflecting the effect of the normal

Fig. 6 Tailored hardening mechanism of a BMG sample with a gradient free volume (FV) content. a1 Schematic diagram of propagation of the shear band initiated from the slow-cooled surface. **a2**, **a3** Schematic diagram of initiation of new shear bands and the subsequent hardening mechanism. **b1** Schematic diagram of blockage of the shear band initiated from the fast-cooled surface. **b2**, **b3** Schematic diagram of initiation of new shear bands, propagation of the shear band initiated from the fast-cooled surface, and the subsequent hardening mechanism.

stress according to α. Shear band propagation proceeded discretely in stages[15]. As it progressed towards the region of high free volume content, α decreased and the influence of normal stress decreased, such that the shear band angle deflected to a higher angle (Fig. 6a1). In particular, as also shown in Fig. 5a, deflection occurred at the 600–2000 μm section of the BMG sample where the values of α and θ_c changed rapidly. When the shear band plane was bent, the stress state became complex. The shear stress was concentrated at the deflection point, such that it was likely to branch the shear band at a tangential angle before the deflection of the shear plane (Fig. 6a2). The branching released the stress in the shear plane, making subsequent propagation more difficult. As deformation continued, apparent hardening occurred because shear bands initiated at the new heterogeneous sites in which the critical shear stress was higher than that in the previous initiation site. As the deformation progressed and a higher stress was applied, the bent shear band additionally propagated; however, in this case, the

shear plane tended to deflect again owing to the differences in α and θ_c (Fig. 6a3). Accordingly, the bend angle of the shear plane increased, and the shear stress was distributed through the branches, such that the shear stress was not properly transferred to the shear band tip. Subsequent hardening occurred through the other new shear bands initiated at the sites with higher critical shear stress.

Figure 6b1-b3 shows schematic illustrations of the propagation of shear bands initiated in the regions of higher free volume content and the subsequent hardening mechanism. When the shear band propagated from a region of high free volume content to a region of low free volume content, the propagation tended to be blocked because the hardness α and the local critical shear stress gradually increased (Fig. 6b1). As shown in Fig. 5a, the shear band was likely to be blocked at a distance of 600–2000 μm from the surface of the BMG sample owing to the rapid change in α. Because shear band propagation was possible only when the effective shear stress of the shear band tip exceeded the local critical shear stress, a

greater uniaxial stress should be applied for subsequent propagation, resulting in apparent hardening under propagation. This allows other shear bands to be easily initiated at new heterogeneous sites rather than via propagation (Fig. 6b2). Thereafter, when the effective shear stress of the shear band tip exceeds the critical shear stress, propagation can occur by deflection at a lower angle in accordance with the α value. This makes the subsequent propagation more difficult as the shear plane is bent, and the shear stress is dispersed through shear band branching (Fig. 6b3).

The shear band propagation was severely disturbed by the 2D gradient rejuvenation state regardless of the initiation position. Because no complete shear band was formed, its initiation and propagation occurred sequentially from the sites with low critical shear stress towards those with high critical shear stress as plastic deformation proceeded. Therefore, an increase in plastic strain accompanied the increase in applied uniaxial stress, and apparent hardening was achieved.

Fracture morphology and tailored hardening

Figure 7a, b shows that the fracture surface morphology was very complex and irregular. Hence, fracturing did not occur in a single complete shear plane, but rather multiple shear planes in different directions were considered to be involved in the fractured region. The fracture surface consisted of major shear planes occupying most of the corresponding area and minor shear planes intersecting the major shear planes. Because the shear stress was dispersed at the deflection point, the effective shear stress applied to each part of the bent shear plane did not exceed the local critical shear stress. Thus, subsequent plastic deformation was generated only by activating shear banding at new initiation sites with higher critical shear stress, which led to considerable apparent hardening. Therefore, more favorable conditions for such hardening were achieved by the induction of a more irregular shear plane. Figure 7c shows schematic diagrams of the interaction of multiple shear planes in different directions during deformation. The major shear planes propagated from regions of low and high free volume contents intersected by the minor shear planes and indirectly connected in a stepped morphology. As a result, the top and bottom of the fracture surfaces were not only different in terms of angle but also did not form smooth a complete shear plane together even at the stage of fracture (Fig. 7d); hence, the hardening rate did not decrease even when the specimen was deformed until fracture.

To summarize, we found that a highly tailored 2D gradient of the free volume concentration in a monolithic BMG, which was achieved by controlling the rejuvenation state, induced sustainable and tailored hardening behavior until fracture. The atomic friction, α, and θ_c varied
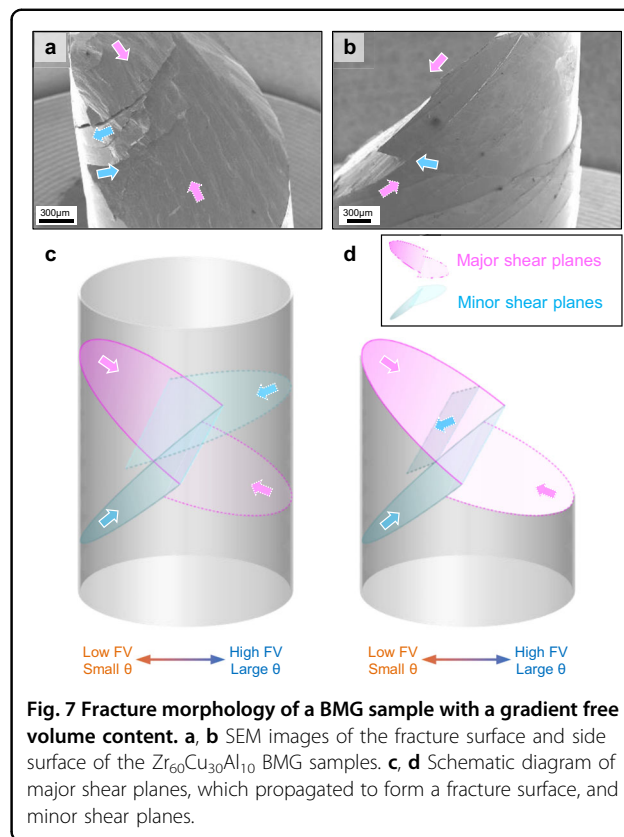

Fig. 7 Fracture morphology of a BMG sample with a gradient free volume content. a, b SEM images of the fracture surface and side surface of the $Zr_{60}Cu_{30}Al_{10}$ BMG samples. **c, d** Schematic diagram of major shear planes, which propagated to form a fracture surface, and minor shear planes.

depending on the local free volume concentration, resulting in bent shear planes. The formation of a complete shear plane transecting the whole specimen was completely blocked. Accordingly, the tailored hardening mechanism of the BMG was maintained throughout the overall plastic deformation. The results of this work provide a new approach for rejuvenation. Specifically, the control of free volume content through annealing, cryogenic treatments, or severe plastic deformation can be used to induce tailored apparent hardening behavior in BMGs. Important issues, such as the fracture conditions, have yet to be investigated; however, this study experimentally demonstrated the alternative hardening mechanism in terms of the intrinsic characteristics of monolithic BMGs without introducing other components to act as hardening elements.

Conflict of interest
The authors declare that they have no conflict of interest.

References

1. Schroers, J. Processing of bulk metallic glass. *Adv. Mater.* **22**, 1566–1597 (2010).
2. Inoue, A. Stabilization of metallic supercooled liquid and bulk amorphous alloys. *Acta Mater.* **48**, 279–306 (2000).
3. Johnson, W. L. Bulk Glass-forming metallic alloys: science and technology. *MRS Bull.* **24**, 42–56 (1999).
4. Ketov, S. & Louzguine-Luzgin, D. Localized shear deformation and softening of bulk metallic glass: stress or temperature driven? *Sci. Rep.* **3**, 2798 (2013).
5. Hofmann, D. C. et al. Designing metallic glass matrix composites with high toughness and tensile ductility. *Nature* **451**, 1085 (2008).
6. Szuecs, F., Kim, C. & Johnson, W. L. Mechanical properties of $Zr_{56.2}Ti1_{3.8}Nb_{5.0}$-$Cu_{6.9}Ni_{5.6}Be_{12.5}$ ductile phase reinforced bulk metallic glass composite. *Acta Mater.* **49**, 1507–1513 (2001).
7. Qu, R., Zhang, Q. & Zhang, Z. Achieving macroscopic tensile plasticity of monolithic bulk metallic glass by surface treatment. *Scr. Mater.* **68**, 845–848 (2013).
8. Qu, R., Calin, M., Eckert, J. & Zhang, Z. Metallic glasses: notch-insensitive materials. *Scr. Mater.* **66**, 733–736 (2012).
9. Qiao, J. et al. Tensile deformation micromechanisms for bulk metallic glass matrix composites: From work-hardening to softening. *Acta Mater.* **59**, 4126–4137 (2011).
10. Wu, Y., Xiao, Y., Chen, G., Liu, C. T. & Lu, Z. Bulk metallic glass composites with transformation-mediated work-hardening and ductility. *Adv. Mater.* **22**, 2770–2773 (2010).
11. Sun, B. et al. Plasticity of ductile metallic glasses: a self-organized critical state. *Phys. Rev. Lett.* **105**, 035501 (2010).
12. Wang, G. et al. Self-organized intermittent plastic flow in bulk metallic glasses. *Acta Mater.* **57**, 6146–6155 (2009).
13. Das, J. et al. "Work-hardenable" ductile bulk metallic glass. *Phys. Rev. Lett.* **94**, 205501 (2005).
14. Liu, Y., Liu, C., Gali, A., Inoue, A. & Chen, M. W. Evolution of shear bands and its correlation with mechanical response of a ductile $Zr_{55}Pd_{10}Cu_{20}Ni_5Al_{10}$ bulk metallic glass. *Intermetallics* **18**, 1455–1464 (2010).
15. Qu, R., Liu, Z., Wang, G. & Zhang, Z. Progressive shear band propagation in metallic glasses under compression. *Acta Mater.* **91**, 19–33 (2015).
16. Lee, J. et al. Deformation and evolution of shear bands under compressive loading in bulk metallic glasses. *Acta Mater.* **54**, 5271–5279 (2006).
17. Zhang, Z., Eckert, J. & Schultz, L. Difference in compressive and tensile fracture mechanisms of $Zr_{59}Cu_{20}Al_{10}Ni_8Ti_3$ bulk metallic glass. *Acta Mater.* **51**, 1167–1179 (2003).
18. Zhou, H. et al. Non-localized deformation in metallic alloys with amorphous structure. *Acta Mater.* **68**, 32–41 (2014).
19. Sun, B. A. et al. Serrated flow and stick–slip deformation dynamics in the presence of shear-band interactions for a Zr-based metallic glass. *Acta Mater.* **60**, 4160–4171 (2012).
20. Flores, K. M. & Dauskardt, R. H. Mode II fracture behavior of a Zr-based bulk metallic glass. *J. Mech. Phys. Solids* **54**, 2418–2435 (2006).
21. Guo, Y., Li, Y., Wu, X. & Wei, Q. A modified criterion for shear band formation in bulk metallic glass under complex stress states. *Mater. Sci. Eng. A* **527**, 2613–2620 (2010).
22. Bruck, H., Christman, T., Rosakis, A. & Johnson, W. L. Quasi-static constitutive behavior of $Zr_{41.25}Ti_{13.75}Ni_{10}Cu_{12.5}Be_{22.5}$ bulk amorphous alloys. *Scr. Metall. Mater.* **30**, 429–434 (1994).
23. Ketkaew, J. et al. The effect of thermal cycling on the fracture toughness of metallic glasses. *Acta Mater.* **184**, 100–108 (2020).
24. Saida, J., Yamada, R. & Wakeda, M. Recovery of less relaxed state in Zr-Al-Ni-Cu bulk metallic glass annealed above glass transition temperature. *Appl. Phys. Lett.* **103**, 221910 (2013).
25. Tong, Y. et al. Structural rejuvenation in bulk metallic glasses. *Acta Mater.* **86**, 240–246 (2015).
26. Wakeda, M., Saida, J., Li, J. & Ogata, S. Controlled rejuvenation of amorphous metals with thermal processing. *Sci. Rep.* **5**, 10545 (2015).
27. Saida, J., Yamada, R., Wakeda, M. & Ogata, S. Thermal rejuvenation in metallic glasses. *Sci. Tech. Adv. Mater.* **18**, 152–162 (2017).
28. Guo, W., Yamada, R. & Saida, J. Rejuvenation and plasticization of metallic glass by deep cryogenic cycling treatment. *Intermetallics* **93**, 141–147 (2018).
29. Pan, J. et al. Extreme rejuvenation and softening in a bulk metallic glass. *Nat. Commun.* **9**, 560 (2018).
30. Wakeda, M. & Saida, J. Heterogeneous structural changes correlated to local atomic order in thermal rejuvenation process of Cu-Zr metallic glass. *Sci. Tech. Adv. Mater.* **20**, 632–642 (2019).
31. Joo, S. H., Kato, H., Gangwar, K., Lee, S. & Kim, H. S. Shear banding behavior and fracture mechanisms of $Zr_{55}Al_{10}Ni_5Cu_{30}$ bulk metallic glass in uniaxial compression analyzed using a digital image correlation method. *Intermetallics* **32**, 21–29 (2013).
32. Gu, X., Poon, S., Shiflet, G. & Lewandowski, J. Compressive plasticity and toughness of a Ti-based bulk metallic glass. *Acta Mater.* **58**, 1708–1720 (2010).
33. Guo, W., Yamada, R. & Saida, J. Unusual plasticization for structural relaxed bulk metallic glass. *Mater. Sci. Eng. A* **699**, 81–87 (2017).
34. Schuh, C. A. & Lund, A. C. Atomistic basis for the plastic yield criterion of metallic glass. *Nat. Mater.* **2**, 449 (2003).
35. Vaidyanathan, R., Dao, M., Ravichandran, G. & Suresh, S. Study of mechanical deformation in bulk metallic glass through instrumented indentation. *Acta Mater.* **49**, 3781–3789 (2001).
36. Baricco, M., Baser, T., Das, J. & Eckert, J. Correlation between Poisson ratio and Mohr–Coulomb coefficient in metallic glasses. *J. Alloy. Compd.* **483**, 125–131 (2009).
37. Caris, J. & Lewandowski, J. Pressure effects on metallic glasses. *Acta Mater.* **58**, 1026–1036 (2010).
38. Hsueh, C.-H., Bei, H., Liu, C. T., Becher, P. F. & George, E. P. Shear fracture of bulk metallic glasses with controlled applied normal stresses. *Scr. Mater.* **59**, 111–114 (2008).
39. Vargonen, M., Huang, L. & Shi, Y. Evaluating Mohr–Coulomb yield criterion for plastic flow in model metallic glasses. *J. Non-Cryst. Solids* **358**, 3488–3494 (2012).
40. Yu, G. et al. Effect of relaxation on pressure sensitivity index in a Zr-based metallic glass. *Mater. Sci. Eng. A* **460**, 58–62 (2007).